nature communications

Article

https://doi.org/10.1038/s41467-025-61074-9

Silver exsolution from Li-argyrodite electrolytes for initially anode-free all-solid-state batteries

Received: 11 January 2025

Accepted: 11 June 2025

Published online: 01 July 2025

Check for updates

Seung Ho Choi[1,6] ✉, Chang Hoon Baek[1,2,6], Jihoon Oh[3], Geung-Jong Lee[1], Minsoo Kim[4], Hyesu Lee[4], Dong-Joo Yoo[5], Yoon Seok Jung[2], KyungSu Kim[1], Ji-Sang Yu[1], Woosuk Cho[1] ✉, Haesun Park[4] ✉ & Jang Wook Choi[3] ✉

Achieving stable cyclability in initially anode-free all-solid-state batteries is challenging due to non-uniform Li (de)plating, especially under practical operating conditions. Here, we introduce a bilayer comprising a silver(Ag)-doped Li-argyrodite electrolyte layer in contact with the undoped Li-argyrodite electrolyte. During charging, electrochemical exsolution of Ag^+ from the silver-doped Li argyrodite forms nanoscale, lithiophilic silver seeds along grain boundaries and in pores where they are accessible for electron transfer. These silver seeds alloy with Li to induce uniform Li plating underneath and return to the electrolyte layer upon Li stripping to enhance the reversibility during cycling. With silver exsolution, a pouch-type full-cell with a volumetric energy density of 1312 Wh L^{-1} (excluding the packaging materials) and areal discharge capacity of 7.0 mAh cm^{-2} at 0.7 mA cm^{-2}, demonstrated stable cycling at a practical stack pressure of 2.0 MPa. This study highlights that Ag^+ diffusion in the Li-argyrodite solid electrolyte and its electrochemical exsolution are an effective strategy for robust, high-energy-density initially anode-free all-solid-state batteries.

The discovery of sulfide-based solid electrolytes, such as Li_6PS_5Cl[1], $Li_{10}GeP_2S_{12}$[2], and $Li_7P_3S_{11}$[3], with various crystallographic structures has hugely advanced all-solid-state Li-ion battery (ASSB) technology, mainly by taking advantage of their high Li-ion conductivities and superior ductility[4–6]. Regarding the cell configuration, initially anode-free ASSBs[7–10] eliminate the need for anode host materials, and represent a notable conceptual advancement in the ASSB field because of their higher energy density, comparative affordability, and simplified manufacturing process. In each initially anode-free cell, during charging, Li ions extracted from the positive electrode pass through the solid electrolyte (SE) layer and are plated onto the anode current collector as metallic Li. However, limited physical contact between the current collector and SE, along with the low affinity for Li of the former, often causes uneven Li plating and eventually fatal short-circuiting[11–13]. Although the high shear modulus of SEs could suppress Li dendrite formation to some extent, the grain boundaries and voids inevitably present in the SE layer could still foster Li dendrite formation[14–17]. Particularly, the susceptibility of grain boundaries with the narrower bandgaps to electron leakage currents accelerates Li dendrite growth. Critically, the external stack pressure governs the formation of voids at the Li metal anode-SE interface; consequently, the interfacial resistance becomes irregular, which also promotes Li dendrite growth[18–22].

[1]Advanced Batteries Research Center, Korea Electronics Technology Institute, Seongnam, Republic of Korea. [2]Department of Chemical and Biomolecular Engineering, Yonsei University, Seoul, Republic of Korea. [3]School of Chemical and Biological Engineering and Institute of Chemical Processes, Seoul National University, Seoul, Republic of Korea. [4]School of Integrative Engineering, Chung-Ang University, Seoul, Republic of Korea. [5]School of Mechanical Engineering, Korea University, Seoul, Republic of Korea. [6]These authors contributed equally: Seung Ho Choi, Chang Hoon Baek. ✉e-mail: sh.choi@keti.re.kr; cho4153@keti.re.kr; parkh@cau.ac.kr; jangwookchoi@snu.ac.kr

The use of lithiophilic metal layers or carbon-based protective layers has been reported as an effective strategy to ensure stable cycling performance[7–9]. Stabilizing the operation of initially anode-free ASSB cells, therefore, remains challenging ad continues to be a barrier to their widespread adoption.

With this challenge in mind, herein, we present an SE bilayer approach for sulfide-based initially anode-free ASSBs. The SE bilayer consists of the well-known Li-argyrodite $Li_6PS_5Cl_{0.5}Br_{0.5}$ and its silver (Ag)-doped analogs ($Li_{6-x}Ag_xPS_5Cl$). During charging, the Ag ions in $Li_{6-x}Ag_xPS_5Cl$ diffuse from their original crystal framework and are electrochemically reduced at the grain boundaries in the SE layer to function as nucleation seeds for Li deposition, followed by the formation of a Li-Ag alloy in the lower SE bilayer. Next, the Ag in the Li deposition layer spreads in the Li metal layer to facilitate uniform and reversible Li deposition and stripping in each cycle. Significantly, Ag ions tend to undergo reduction where electrons are inherently accessible in the SE layer; thus, the reduced Ag itself naturally plays a role in supplementing electron transfer for facile Li deposition during each charging process. The sequential processes for uniform Li plating in the anode, initiated by Ag exsolution, are graphically summarized in Fig. 1a. This SE bilayer approach enabled initially anode-free half-cells to be sustained for 1000 cycles at 1.0 mA cm^{-1} with 1.0 mAh cm^{-2}, without short-circuiting or increased polarization. Even pouch-type ASSB full-cells with an unusually high areal capacity of 7.0 mAh cm^{-2} demonstrated reliable cycling behavior under a practical operating pressure of 2.0 MPa. This work reveals electrochemically induced Ag exsolution along grain boundaries as a useful concept for realizing highly reliable initially anode-free ASSBs with high energy densities.

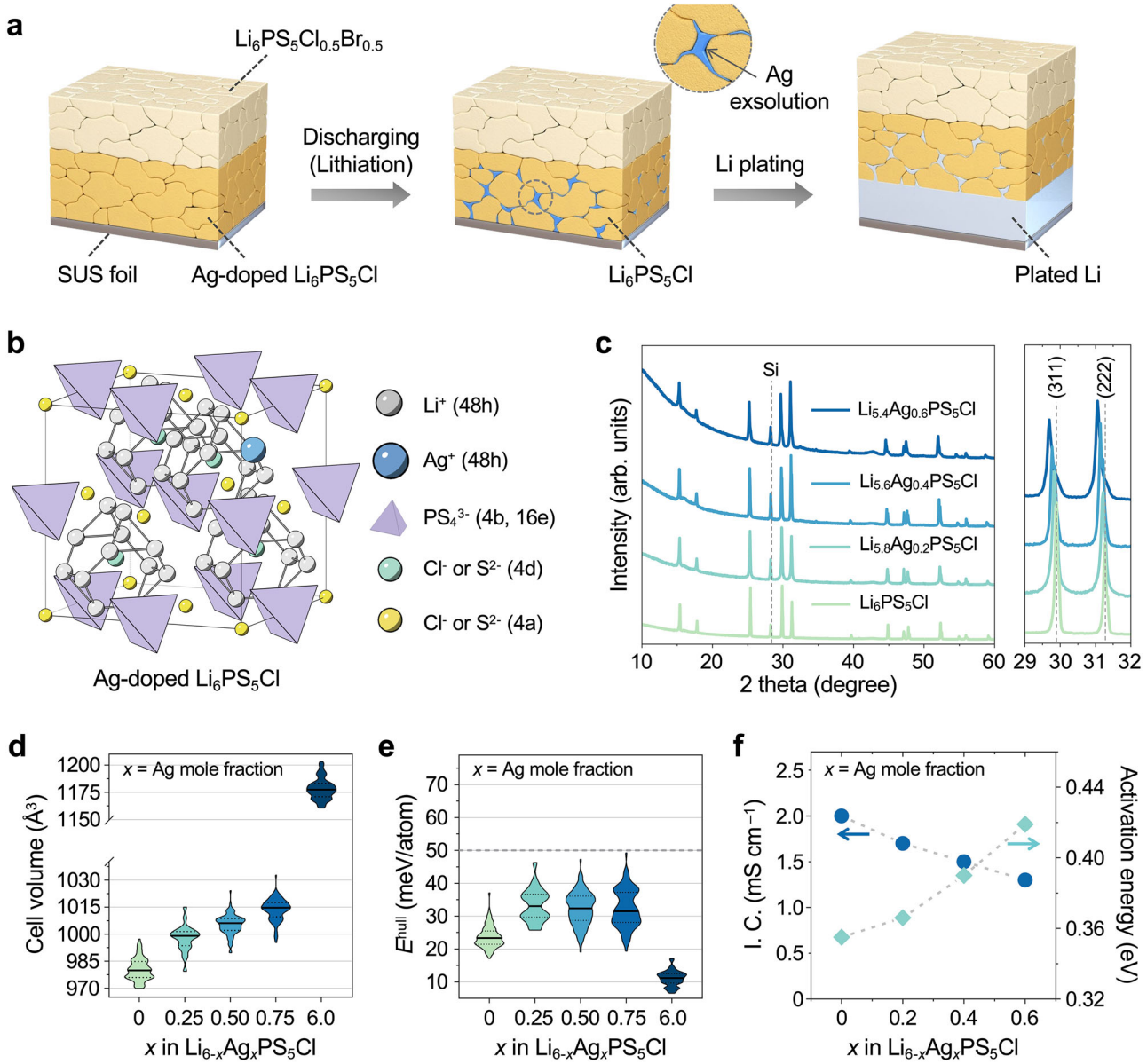

Fig. 1 | Ag exsolution-induced Li plating mechanism and $Li_{6-x}Ag_xPS_5Cl$ SEs. **a** Schematic of the proposed Li plating mechanism involving Ag exsolution along grain boundaries and in pores. **b** Crystal structure in which the Li sites of Li_6PS_5Cl are partially occupied by Ag^+ dopant ions. Li^+ and Ag^+ are represented by gray and blue spheres, respectively. **c** XRD patterns of the synthesized $Li_{6-x}Ag_xPS_5Cl$ SEs ($x = 0$, 0.2, 0.4, and 0.6). **d**, **e** Violin plots with regard to (**d**), cell volume and (**e**), phase stability (energy above the hull, E^{hull}) for the simulated $Li_{6-x}Ag_xPS_5Cl$ structures ($x = 0$, 0.25, 0.5, 0.75, and 6.0). The solid line within each violin represents the median, and the dotted lines indicate the first and third quartiles. The sample sizes in (**d, e**) are $n = 100$ for $x = 0$, 0.50, 0.75, and 6.0, and $n = 24$ for $x = 0.25$. **f** Ionic conductivities (I. C.) at 293 K and activation energies of the $Li_{6-x}Ag_xPS_5Cl$ SEs.

Results

Synthesis and analysis of the Ag-doped Li-argyrodite electrolyte

Figure 1b illustrates the Ag-doped Li_6PS_5Cl argyrodite structure. Within this framework, the Li ions (48 h or 24 g sites) are distributed along the cage-like structures, with inter-cage hopping allowing the long-range diffusion of Li ions[23,24]. Likewise, Ag ions that substituted Li ions could diffuse along the same Li ion paths. The $Li_{6-x}Ag_xPS_5Cl$ SEs ($x = 0$, 0.2, 0.4, and 0.6) were synthesized using conventional heat treatment (Supplementary Fig. 1; details in Methods). Scanning electron microscopy (SEM) imaging (Supplementary Fig. 2) revealed that the synthesized samples have particle sizes ranging from 1 to 3 µm, and SEM-energy dispersive spectroscopy (EDS) analysis confirmed the uniform distributions of S and Ag without aggregation. The XRD patterns verified that all samples have argyrodite structures without impurities (Fig. 1c). To elucidate the structural changes induced by Ag^+ doping, we analyzed the (311) and (222) planes (the peaks at 29.8 and 31.3°), which are primarily associated with Cl^-/S^{2-} and Li^+ occupations, respectively (Supplementary Fig. 3)[25]. The enlarged XRD patterns (Fig. 1c, right) showed that both peaks shifted to lower angles, attributable to the larger ionic radius of Ag^+ (1.15 Å) compared to that of Li^+ (0.6 Å). The intensity ratio of the (222) to (311) planes progressively increased with the addition of Ag^+, suggesting that Ag^+ preferentially occupies the (222) plane. A similar trend emerged for the Ag-doped Li_3PS_4 electrolyte (see Supplementary Fig. 4). Rietveld refinement analysis of the XRD patterns (Supplementary Fig. 5) revealed progressive expansion of the cubic lattice parameters from 9.845 in Li_6PS_5Cl to 9.856, 9.880, and 9.910 Å in the $Li_{6-x}Ag_xPS_5Cl$ SEs ($x = 0.2$, 0.4, and 0.6), respectively.

In contrast, X-ray photoelectron spectroscopy (XPS) analysis of the Ag 3*d* spectra of $Li_{6-x}Ag_xPS_5Cl$ (Supplementary Fig. 6) revealed consistent peaks at 367.9 and 374.0 eV for all the compositions. These peaks are ascribed to the Ag−S bond in the commonly present Ag_2S[26]. Similarly, the XPS P 2*p* and S 2*p* spectra also consistently displayed peaks attributed to the PS_4^{3-} polyhedra for all the compositions[27]. Collectively, the SEM, XRD, and XPS analyses corroborate the successful doping of the $Li_{6-x}Ag_xPS_5Cl$ lattice with Ag^+ without perturbation of the intrinsic argyrodite framework.

Density functional theory (DFT) calculations enabled an examination of the effect of different amounts of Ag in $Li_{6-x}Ag_xPS_5Cl$ ($x = 0$, 0.25, 0.5, and 0.75) on the cell volume and structural stability. Simulations were performed for $x = 0$, 0.25, 0.5, and 0.75 in $Li_{6-x}Ag_xPS_5Cl$, which differ from the experimental compositions, to balance computational feasibility and physical accuracy. Figure 1d presents the calculated cell volumes as violin plots, where the horizontal width corresponds to the frequency of the structure with the given volume. The results also indicate that higher Ag content increases the average lattice parameters. To assess the influence of Ag doping on the thermodynamic structural stability, the energy above the convex hull (E^{hull}) was calculated (Fig. 1e). Structures with $E^{hull} < 50$ meV/atom are considered to be metastable yet synthetically viable[28,29]. The 100 predicted $Li_{6-x}Ag_xPS_5Cl$ structures all meet this criterion, suggesting that Ag^+ doping does not significantly impair the structural stability. Notably, Ag_6PS_5Cl was predicted to be more stable than Li_6PS_5Cl and intermediate Ag-doped compositions ($x < 6$). Furthermore, other mono- and di-valent cations (e.g., Cu^+, K^+, Na^+, and Mg^{2+}, Zn^{2+}) were also predicted to be synthetically feasible, suggesting the possibility of synthesizing SEs containing diverse cations (Supplementary Table 1). The ionic conductivities of $Li_{6-x}Ag_xPS_5Cl$ ($x = 0$, 0.2, 0.4, 0.6) at 293 K (Fig. 1f and Supplementary Fig. 7a) were 2.0, 1.7, 1.5, and 1.3 mS cm^{-1}, respectively, implying that the ionic conductivity decreases slightly with increasing Ag content. Consistently, their activation energies (Supplementary Fig. 8), determined by measuring their ionic conductivities at different temperatures, were 0.36, 0.37, 0.39, and 0.42 eV, respectively. In addition, the electronic conductivities of the given compositions (Supplementary Fig. 7b) were measured to be 2.3, 1.8, 1.6, and 1.3×10^{-10} S cm^{-1}, respectively, revealing that their electrically insulating characteristics were maintained.

Electrochemically induced Ag exsolution

To investigate the effect of the electrochemically induced Ag exsolution from the $Li_{5.4}Ag_{0.6}PS_5Cl$ SE on the cell performance, we prepared two half-cells without and with this Ag-doped SE layer (Cell A and Cell B, respectively, in Fig. 2a). Figure 2b displays their initial discharge (lithiation) profiles. Upon discharge, whereas the potential of Cell A instantly dropped to 0 V without any sign of electrochemical reactions, Cell B exhibited a potential profile indicative of distinct redox reactions originating from the $Li_{5.4}Ag_{0.6}PS_5Cl$ layer. Notably, the color of Cell B turned from brown to black at 1.2 V (inset of Fig. 2b), presumably from the formation of metallic Ag. Moreover, the capacity delivered until 1.2 V (~ 48.1 mAh g^{-1}) is consistent with the theoretical capacity of $Li_{5.4}Ag_{0.6}PS_5Cl$ (48.9 mAh g^{-1}) corresponding to its complete Ag exsolution. Upon full discharge to 0.005 V, Cell B with the 10 µm-thick $Li_{5.4}Ag_{0.6}PS_5Cl$ layer delivered a specific capacity of 235.7 mAh g^{-1} (0.51 mAh cm^{-2}). The capacity delivered after point ii is attributed to Ag-Li alloying reactions, as described below.

Using ex-situ XRD analysis, we monitored the structural evolution of $Li_{5.4}Ag_{0.6}PS_5Cl$ during discharge. Figure 2c presents the XRD patterns at the specific potentials marked in Fig. 2b. At point i (OCV), the XRD pattern verified the argyrodite structure of $Li_{5.4}Ag_{0.6}PS_5Cl$. At point ii (1.2 V), the presence of the characteristic peaks of both Li_6PS_5Cl and Ag metal confirmed the formation of metallic Ag through a redox reaction evident from the plateau at 1.8 V. As the discharge proceeded to points iii (0.12 V), iv (0.04 V), and v (0.005 V), the formed Ag progressively alloyed with Li to form Ag-Li alloys[30–32] with increasing Li contents, while the patterns characteristic of the Li_6PS_5Cl framework remained consistent. This infers that the Li-ion conductive pathways in the SE framework are largely maintained even after Ag exsolution. Additionally, enlargement of the XRD peaks near 30° (Fig. 2c, right) showed that the relative peak ratio of $Li_{5.4}Ag_{0.6}PS_5Cl$ between the (311) and (222) planes at OCV (point i) reversed as soon as Ag ions were extracted at point ii and thereafter, until the XRD pattern eventually resembled that of Li_6PS_5Cl. This phenomenon can be explained by the substitution of Ag ions in the (222) plane by Li ions and can, in turn, be used as a marker for detecting the endpoint of Ag exsolution.

The structural stability of Li_6PS_5Cl and $Li_{5.25}Ag_{0.75}PS_5Cl$ was further elucidated as a function of the applied potential by focusing on their likelihood to decompose[28,33]. DFT calculations indicated that the decomposition energies of both compositions remained extremely low ($|E_D| < 25$ meV/atom) in the potential range 1.72−2.14 V (Fig. 2d). This is well aligned with the aforementioned XRD result that the structural integrity of $Li_{5.4}Ag_{0.6}PS_5Cl$ is preserved throughout the exsolution of Ag, which mostly takes place at the potential plateau of 1.8 V (Fig. 2b). Nonetheless, below 1.71 V, the absolute value of E_D tends to increase steadily, implying that the surfaces and grain boundaries of Li_6PS_5Cl and $Li_{5.4}Ag_{0.6}PS_5Cl$ inevitably decompose to yield byproducts[27,33,34]. The plausible decomposition products of $Li_{5.25}Ag_{0.75}PS_5Cl$ at the different potential levels were suggested by DFT calculations, and similar analyses were performed for the other $Li_{6-x}Ag_xPS_5Cl$ ($x = 0$, 0.25, 0.5, and 6) compositions (Supplementary Fig. 9).

We measured the ionic and electronic conductivities of the $Li_{5.4}Ag_{0.6}PS_5Cl$ electrode at OCV and 1.2 V. Whereas the ionic conductivities of $Li_{5.4}Ag_{0.6}PS_5Cl$ at these points were similar (1.3 and 1.0 mS cm^{-1}, respectively; Fig. 2e and Supplementary Fig. 10 and Note 1), the electronic conductivities were completely distinct (1.5×10^{-10} and 2.5×10^{-3} S cm^{-1}; Supplementary Fig. 11). The similar ionic conductivities confirmed the sustained framework of the SE after Ag exsolution. On the other hand, the surge in the electronic conductivity at 1.2 V is linked to the formation of Ag metal along the electron

https://doi.org/10.1038/s41467-025-61074-9

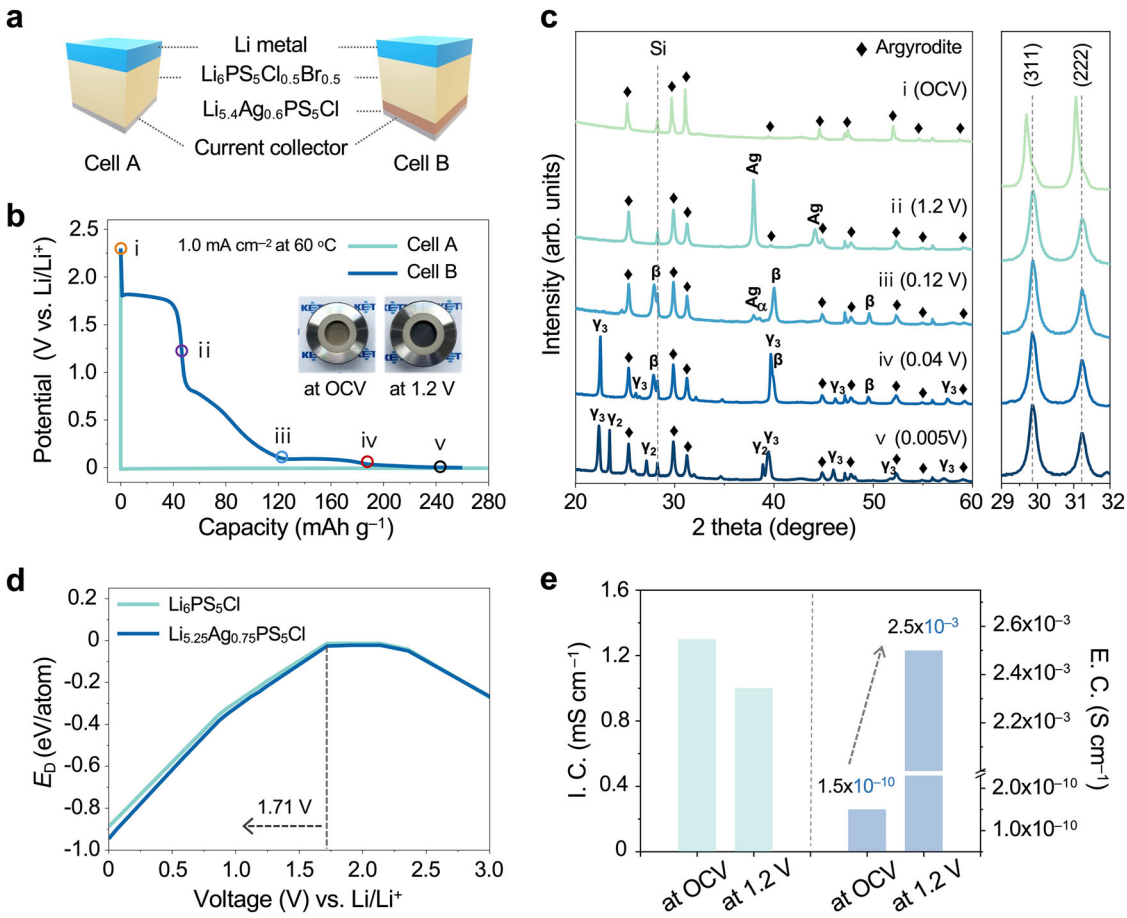

Fig. 2 | Ag exsolution from the Ag-doped Li-argyrodite SE. a Schematic illustration of the two half-cell configurations paired with Li metal. **b** Initial galvanostatic discharge profiles of the cells shown in (**a**) when scanned at 1.0 mA cm^{-2} at 60 °C. **c** Ex-situ XRD patterns of $Li_{5.4}Ag_{0.6}PS_5Cl$ extracted from Cell B at the specific potentials marked in (**b**). The peaks denoted as α, β, γ_3, and γ_2 are characteristic of Ag, LiAg, Li_9Ag_4, and $Li_{10}Ag_3$, respectively. **d** Decomposition energy (E_D) of Li_6PS_5Cl and $Li_{5.25}Ag_{0.75}PS_5Cl$ as a function of the applied potential. **e** Ionic and electronic conductivities (I. C. and E. C.) of the $Li_{5.4}Ag_{0.6}PS_5Cl$ electrode at open circuit voltage (OCV) and discharged at 1.2 V.

transfer pathways within the SE layer. The ionic and electronic conductivities of $Li_{5.8}Ag_{0.2}PS_5Cl$ and $Li_{5.6}Ag_{0.4}PS_5Cl$ followed consistent trends (Supplementary Figs. 10, 11).

Reversible Li plating enabled by the SE bilayer

The effect of Ag exsolution on the electrochemical performance was additionally evaluated by fabricating Li|SUS pellet-type half-cells with the $Li_6PS_5Cl_{0.5}Br_{0.5}$ | $Li_{6-x}Ag_xPS_5Cl$ bilayer. The half-cell with the $Li_6PS_5Cl_{0.5}Br_{0.5}$ | $Li_{5.4}Ag_{0.6}PS_5Cl$ bilayer demonstrated the best cycling performance, with average Coulombic efficiency (CE) of 99.7% for 1000 cycles at 60 °C without increasing the polarization significantly (Fig. 3a and Supplementary Fig. 12). Importantly, the critical current density (CCD) value of the Li|$Li_6PS_5Cl_{0.5}Br_{0.5}$ | $Li_{5.4}Ag_{0.6}PS_5Cl$ | SUS half-cell was as high as 6.0 mA cm^{-2} (Fig. 3b). Furthermore, the given cell operated stably for 150 cycles at 1.0 mA cm^{-2} with a high areal capacity of 5.0 mAh cm^{-2} (Supplementary Fig. 13). The electrochemically formed Ag particles also facilitated reversible Li plating at 30 °C (Supplementary Fig. 14). To demonstrate the impact of the electrochemically induced Ag exsolution more explicitly, a slurry-coating process was used to prepare a composite electrode composed of Li_6PS_5Cl and Ag nanoparticles such that its Ag nanoparticle content was equivalent to that of $Li_{5.4}Ag_{0.6}PS_5Cl$. SEM-EDS visualization of this electrode indicated severe Ag aggregation (Supplementary Fig. 15). Moreover, the electronic conductivity of this composite electrode (1.0×10^{-7} S cm^{-1}) was far lower than that of the $Li_{5.4}Ag_{0.6}PS_5Cl$ electrode after Ag exsolution. This control electrode validates the critical role of Ag exsolution in obtaining well-distributed Ag seeds and enhanced electronic conductivity.

The Li plating beneath the SE bilayer was probed by conducting ex-situ cross-sectional SEM-EDS analyses at different points during the first cycle. In contrast to the OCV state (Fig. 3c), discharge at 0.005 V resulted in the formation of alloyed Ag-Li along the grain boundaries and in pores in the $Li_{5.4}Ag_{0.6}PS_5Cl$ layer (Fig. 3d). These alloyed deposits are clearly captured in the magnified SEM-EDS images (Fig. 3e). The early-stage Ag exsolution was examined by visualizing the same electrode using SEM-EDS after only 1 min of discharge (Supplementary Fig. 16). Even at this early stage, exsoluted Ag was observed near the SUS current collector immediately after being reduced, whereupon Ag exsolution propagated progressively throughout the $Li_{5.4}Ag_{0.6}PS_5Cl$ layer to create connected electron transfer pathways. Upon Li plating at 5.0 mAh cm^{-2}, a compact layer of Li metal formed between the SE bilayer and SUS current collector (Fig. 3f). At this point, Ag was detected throughout the plated Li, indicating the formation of a Li-rich Ag-Li solid-solution as a result of the diffusion of Ag into the plated Li layer[31,32,35]. By contrast, severe Li dendrite growth was observed in a control cell with the $Li_6PS_5Cl_{0.5}Br_{0.5}$ | Li_6PS_5Cl bilayer when discharged at 5.0 mAh cm^{-2}, thereby revalidating the crucial role of exsoluted Ag to ensure uniform Li plating (Supplementary Fig. 17). Intriguingly, Li plating at 5.0 mAh cm^{-2} resulted in the formation of unfilled voids in the Li_6PS_5Cl layer (Supplementary Fig. 18a), whereas

https://doi.org/10.1038/s41467-025-61074-9

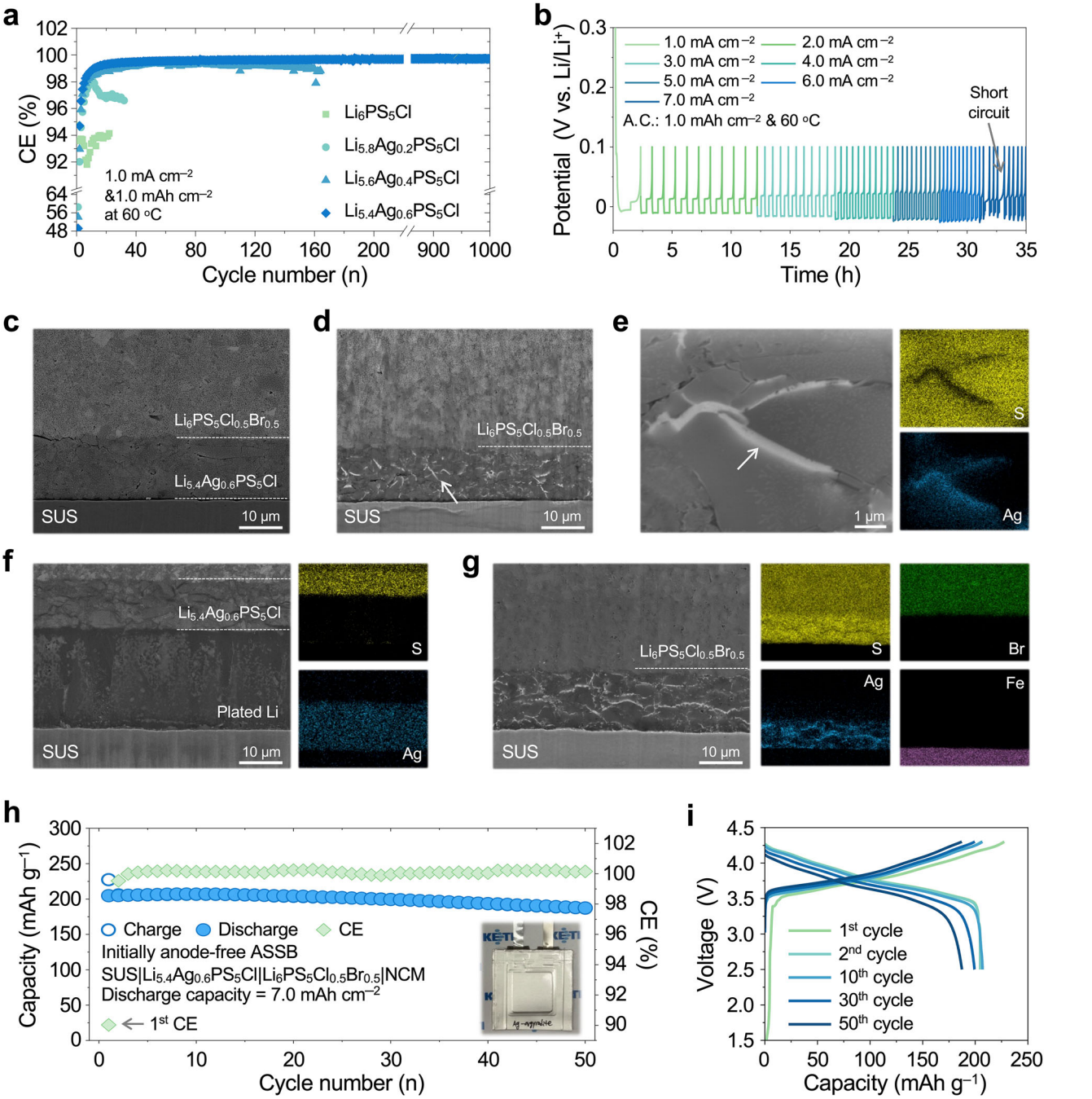

Fig. 3 | Cell performance with the SE bilayer. a Coulombic efficiency (CE) of Li|$Li_6PS_5Cl_{0.5}Br_{0.5}$|$Li_{6-x}Ag_xPS_5Cl$|SUS half-cells at 60 °C ($x = 0$, 0.2, 0.4, and 0.6). **b** Critical current density measurement of the Li|$Li_6PS_5Cl_{0.5}Br_{0.5}$|$Li_{5.4}Ag_{0.6}PS_5Cl$|SUS half-cell. The current density was varied for both charge and discharge, and the areal capacity was kept constant at 1.0 mAh cm^{-2}. **c**–**g** Cross-sectional SEM-EDS images at (**c**) OCV, after (**d**,**e**) discharge at 0.005 V, (**f**) Li plating at 5.0 mAh cm^{-2}, and (**g**) Li stripping to 0.1 V in the first cycle. The current density and operating temperature were fixed at 1.0 mA cm^{-2} and 60 °C, respectively. **h** Cycling performance and (**i**) Voltage profiles of the pouch-type initially anode-free ASSB at 60 °C. The capacities in (**h**, **i**) refer to discharge capacities.

the voids that formed in its $Li_{5.4}Ag_{0.6}PS_5Cl$ counterpart were completely filled with alloyed Ag-Li and metallic Li (Supplementary Fig. 18b) owing to the exsoluted Ag seeds. During subsequent Li stripping, the grain boundaries and voids in the $Li_{5.4}Ag_{0.6}PS_5Cl$ layer remained filled with alloyed Li-Ag (Fig. 3g), implying that Ag was unlikely to migrate back into the lattice of Li_xPS_5Cl.

The robust performance of the operational concept based on Ag exsolution was demonstrated in a practically viable cell setting by fabricating pouch-type full-cells for galvanostatic assessment (Fig. 3h). A cross-sectional SEM image of a pouch cell with a 35 μm-thick SE bilayer is shown in Supplementary Fig. 19. This pouch cell delivered an initial reversible capacity of 205 mAh g^{-1} (equivalent to 7.0 mAh cm^{-2}) at 0.7 mA cm^{-2} under stack pressure of 2.0 MPa (Fig. 3i), and also demonstrated stable cycling retention of 95.0% after 50 cycles at 0.7 mA cm^{-2} and 60 °C. The discharge capacity at 30 °C under 2.0 MPa was 198.1 mAh g^{-1} (equivalent to 7.8 mAh cm^{-2}) and stable cycling at 0.7 mA cm^{-2} (0.1 C) was demonstrated with 87.4% of the initial capacity retained after 50 cycles (Supplementary Fig. 20). Compared to previously reported initially anode-free pouch cells (Supplementary Table 2), the current work demonstrated stable operation at 30 and

https://doi.org/10.1038/s41467-025-61074-9

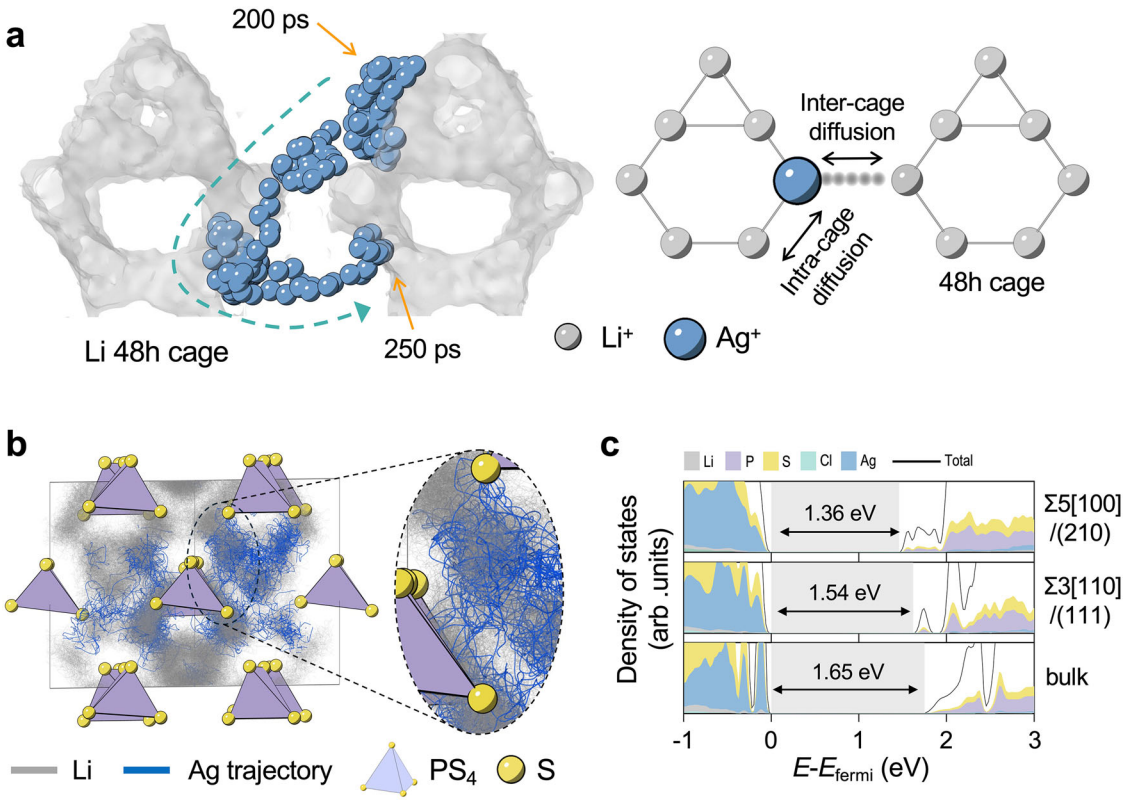

Fig. 4 | Computational simulations of Ag exsolution. a AIMD-simulated Li ion distribution map (gray) of the equal probability density over 400 ps, along with the Ag^+ diffusion trajectory (blue) spotted at every 100 fs for 50 ps. (Right) Schematic representation of intra-cage and inter-cage diffusion pathways across the Li 48 h cage face. The gray and blue spheres represent Li and Ag atoms, respectively. **b** AIMD-simulated inter-cage diffusion trajectory maps of Li and Ag ions in larger crystallographic dimensions. **c** Calculated partial density of state of the bulk and grain boundary structures of $Li_{5.25}Ag_{0.75}PS_5Cl$.

60 °C with a high areal capacity of 7.0 mAh cm^{-2}. Dismantling of the cell in the 50% state of discharge in the first cycle and detachment of the SUS current collector from the SE bilayer (Supplementary Fig. 21a) revealed that the plated Li layer uniformly covered the entire electrode area. Consistent with the results in Fig. 3f, the cross-sectional SEM-EDS analysis confirmed the uniform distribution of Ag throughout the plated Li layer of the pouch cell in this state of discharge (Supplementary Fig. 21b). Notably, the energy density was calculated to be 1312 Wh L^{-1}, excluding the packaging materials (Supplementary Table 3). Overall, the series of results portrays a consistent picture that the $Li_{5.4}Ag_{0.6}PS_5Cl$ layer, after Ag exsolution, was transformed into an ideal lithophilic structure that promoted uniform Li plating in the initially anode-free ASSB cell scheme over repeated cycles. On a separate note, in terms of Ag distribution, the Ag at the grain boundaries of the $Li_{5.4}Ag_{0.6}PS_5Cl$ layer is expected to be more uniformly distributed than previously reported metallic Ag in the composite protection layer, whose distribution cannot always be warranted.

Kinetic requirements for Ag exsolution of the Li-argyrodite

Ab-initio molecular dynamics (AIMD) was used to simulate the diffusion of Li and Ag ions within the argyrodite framework (Supplementary Data 1). In Fig. 4a, the gray clouds represent Li^+ probability density iso-surfaces generated by simulating Li^+ diffusion for 400 ps. This Li^+ iso-surface map indicates the Li occupation sites (48 h) in the framework and thus the overlapping footprint. Along with this Li^+ iso-surface, the simulated Ag^+ trajectory between 200 ps and 250 ps (Fig. 4a) points to the feasibility of Ag^+ engaging in inter-cage crossover: a Ag ion positioned in the cage on the right at 200 ps crosses to the cage on the left and then returns to that on the right at 250 ps. Figure 4b depicts the Li and Ag ion trajectories over larger crystallographic dimensions for 400 ps. The convergence of the Li^+ trajectories over this period to cage-like geometries reflects the high likelihood of intra-cage hopping[23,24,36]. These trajectories also suggest the possibility of inter-cage hopping, although less frequent (lighter gray) than intra-cage hopping. Moreover, the Ag^+ trajectories largely overlap with those of Li^+, implying that Ag^+ follows similar pathways for its diffusion towards exsolution. In the same vein, magnification of the Ag^+ line trajectories (Fig. 4b, inset) portrays the oscillating diffusion of Ag^+ between the cages. On the other hand, the mean squared displacement calculations indicate that P, S, and Cl atoms remain at their original crystallographic positions, confirming the structural stability of the argyrodite framework. (Supplementary Fig. 22) In fact, a recent study[37] also suggested the possibility of Cu^+ diffusion along the Li^+ trajectories in the Li_6PS_5Cl, supporting our rationale for Ag exsolution via the Li^+ trajectories.

We additionally investigated the electronic structures of the bulk and grain boundary models (Supplementary Fig. 23 and Note 2), as exemplified by the partial density of states (pDOS) of the bulk and grain boundaries in $Li_{5.25}Ag_{0.75}PS_5Cl$ (Fig. 4c). The calculated bandgap energies for the Σ3[110]/(111) and Σ5[100]/(210) grain boundaries are 1.54 and 1.36 eV, respectively, both lower than the bulk bandgap of 1.65 eV. The narrower bandgaps of the grain boundary structures are attributed[38,39] to the presence of local defects and high-index surfaces. Although these narrowed bandgaps do not offer band-like conduction, they may explain the preferential Ag exsolution along the grain boundaries, preceded by the reduction of Ag^+. These results once again attest to the foundational role of the well-distributed, lithiophilic Ag seeds at the nanoscale, facilitated by Ag exsolution, to realize uniform reversible Li (de)plating.

In summary, despite their unparalleled theoretical energy density, warranting uniform Li (de)plating is still nontrivial in initially anode-

free ASSBs, particularly under practical stack conditions. We introduced electrochemically induced Ag exsolution from a Ag-doped Li-argyrodite layer to effectuate the generation of well-distributed nanoscale Ag seeds. Notably, Ag exsolution occurs via ion diffusion and electrochemical reduction, preferentially along grain boundaries where electron transfer is readily available. These exsoluted Ag seeds promote uniform Li (de)plating to enable robust cycling at a practically workable pressure of 2.0 MPa. Moreover, the thin SE bilayer (only 35 μm thick) offers energy density in excess of 1300 Wh L^{-1} for pouch-type ASSB cells. This study highlights the importance of conductive nucleation seeds for the highly reliable operation of high energy-density initially anode-free ASSB cells, a criterion that is ideally met with exsoluted Ag seeds along grain boundaries in the SE framework.

Methods

Synthesis of solid electrolytes

The Ag-doped solid electrolytes were synthesized by combining stoichiometric amounts of Li_2S (99.98%, no.213241, Sigma Aldrich), P_2S_5 (99%, no.232106, Sigma Aldrich), LiCl (99%, no.746460, Sigma Aldrich), LiBr (99%, no.213225, Sigma Aldrich) and AgCl (99.9%, no. 227927, Sigma Aldrich) powders in a ball mill for pulverization at 450 rpm for 2 h in a ZrO_2 jar with 5 mm ZrO_2 balls (Pulverisette 7, Fritsch). The mechanically mixed powders were post-treated at 550 °C for 6 h in a quartz glass tube oven under vacuum. The $Li_6PS_5Cl_{0.5}Br_{0.5}$ (LPSCl) solid electrolyte was prepared by the same process, without the addition of AgCl. The size of the powder particles was further reduced by ball milling in heptane (99%, no. 246654, Sigma Aldrich) at 200 rpm for 2 h in the ZrO_2 jar with ZrO_2 balls.

Fabrication of initially anode-free ASSB cells

The solid electrolyte layer was prepared by dispersing $Li_{6-x}Ag_xPS_5Cl$ powder and styrene-butadiene rubber binder (M_n ~ 60000, SBR, Kumho Petrochemical) in butyl butyrate (98%, no.281964, Sigma Aldrich, 97:3 by weight) to form a slurry. The prepared slurry was cast onto a stainless steel (SUS) current collector to a thickness of 15 μm. The $Li_{6-x}Ag_xPS_5Cl$ layer was dried in a hot-dry oven at 80 °C for 1 h and subsequently at 100 °C for 2 h under vacuum. The $Li_6PS_5Cl_{0.5}Br_{0.5}$ layer was prepared similarly by combining $Li_6PS_5Cl_{0.5}Br_{0.5}$ powder and SBR (97:3 by weight). The solid content of the slurry was 65%. The resulting slurry was cast onto a PTFE film to a thickness of 50 μm using the doctor blade method, which decreased to approximately 40 μm after drying. The positive electrode was prepared by dispersing $LiNbO_3$-coated $LiNi_{0.8}Co_{0.1}Mn_{0.1}O_2$, Li_6PS_5Cl (Posco-JK Co.), carbon black (Super C65, Timcal), and nitrile-butadiene rubber (M_n ~ 250000, NBR, Kumho Petrochemical) in butyl butyrate in an 80:17:1.5:1.5 weight ratio. The slurry was mixed using a Thinky Mixer at 2000 rpm for 10 min. This mixture was cast onto an aluminum current collector at a thickness of 450 μm using the doctor blade method. The solvent was removed in a vacuum chamber at 100 °C for 2 h. The loading of the active material on the positive electrode was approximately 50 mg cm^{-2}.

For the fabrication of the half-cells including a $Li_{6-x}Ag_xPS_5Cl$ layer (x = 0, 0.2, 0.4, 0.6), 150 mg of $Li_6PS_5Cl_{0.5}Br_{0.5}$ was cold-pressed at 50 MPa using a PEEK mold with a diameter of 13 mm. The 10 μm-thick $Li_{6-x}Ag_xPS_5Cl$ layer cast on the SUS collector was placed on one side of the $Li_6PS_5Cl_{0.5}Br_{0.5}$ pellet and pressed at 500 MPa for 1 min using a titanium mold. The thickness of the LPSCl membrane was estimated to 700 μm. After pressing, the Li film with a thickness of 100 μm on SUS foil was placed on the other side of the $Li_6PS_5Cl_{0.5}Br_{0.5}$ pellet, and the assembly was placed in a home-made uniaxial pressure cell and tightened at 20 MPa. The cells were rested at the set temperature (30 or 60 °C) for 3 h before cycling. To fabricate a pouch-type initially anode-free full-cell, the freestanding $Li_6PS_5Cl_{0.5}Br_{0.5}$ layer with a thickness of approximately 40 μm was delaminated from the PTFE film. The dimensions of the positive electrode, $Li_6PS_5Cl_{0.5}Br_{0.5}$ layer, and $Li_{6-x}Ag_xPS_5Cl$ layer were 20 mm × 20 mm, 24 mm × 24 mm, and 22 mm × 22 mm, respectively. All the electrodes were stacked and packed into a pouch film. After sealing the pouch cell under vacuum, it was pressurized at 500 MPa and 80 °C by the warm isostatic pressing (WIP) process (ISA-W50-6000, Ilshin Autoclave). All of the cells were fabricated in a dry room with a dew point below − 50 °C and tested in an environmental chamber maintained at either 30 ± 0.5 °C or 60 ± 0.5 °C.

Electrochemical characterization

The half-cell test (N = 1 ~ 3 cells for each condition) was conducted by allowing Li plating to proceed for either 1 h or 5 h at a current density of 1.0 mA cm^{-2}. The cut-off potential for Li stripping was set at 0.1 V (vs. Li/Li^+), using a battery cycler (WBCS 3000, WonATech). The Coulombic efficiency in half-cells is defined as the Li plating capacity divided by the Li stripping capacity in each cycle. The cyclability of the pouch-type full-cells (N = 2 cells) was galvanostatically assessed at 0.7 mA cm^{-2} in constant current (CC) mode for both charge and discharge in the voltage range of 2.5–4.3 V. A current density of 7.0 mA cm^{-2} was used as 1 C. The Coulombic efficiency in full-cells is defined as the charging capacity divided by the discharging capacity in each cycle. The stack pressure of the pouch cells during cycling was maintained at 2.0 MPa. No formation cycles were included for any of the cell tests. The impedance data were recorded on an impedance analyzer (Bio-Logic, VSP-300) in the frequency range of 7 MHz–0.1 Hz at the amplitude of 15 mV. A total of 79 data points were collected for each measurement. The DC polarization data were obtained using the same analyzer by sequentially applying potentials from ± 5 mV to ± 300 mV, each applied for 20 s.

Characterization

Scanning electron microscopy-energy dispersive spectroscopy (SEM-EDS) images were acquired using a JSM-IT200 instrument (JEOL) in a dry room with a dew point below − 50.0 °C at an accelerating voltage of 15 kV. For cross-sectional SEM imaging, cells were dissected using a cross-section polisher (JEOL, IB-19520CCP) at 5.0 kV for 1 h. X-ray diffraction (XRD) patterns were collected on a PANalytical Empyrean diffractometer with Cu-Kα radiation at a scan rate of 5° min^{-1} and a step size of 0.026°. A home-made holder with a polyimide cover was employed to protect the samples from moisture while they were being loaded into the XRD chamber. The Rietveld refinement of the XRD patterns was performed using the FullProf software. Chemical information about the synthesized solid electrolytes was obtained using X-ray photoelectron spectroscopy (XPS, VG Multilab ESCA system, 220i) installed in a dry room. XPS measurements were conducted using an Al Kα source (1486.6 eV) with a spot size of 400 μm and an energy step size of 0.1 eV. Electrodes for all ex-situ analyses were prepared by disassembling the cells without any washing or polishing in a dry room with a dew point of − 50 °C.

Computational details

DFT calculations were conducted using the Vienna ab initio simulation package (VASP) to investigate the thermodynamic stability and the electrochemical exsolution of $Li_{6-x}Ag_xPS_5Cl$[40]. The core-valence electron interactions were modeled using projector-augmented wave potentials with a plane-wave cutoff energy of 520 eV[41]. The Perdew–Burke–Ernzerhof exchange-correlation functional within the generalized gradient approximation was employed[42]. The Γ-point centered k-point mesh of 2 × 2 × 2 was used, and an electronic convergence criterion of 10^{-5} eV was used for all calculations.

Structural models of $Li_{6-x}Ag_xPS_5Cl$ (x = 0.25, 0.50, 0.75) were generated using Python Materials Genomics (pymatgen)[43]. A total of 100 structures were derived from the crystallographic information file, with partial Ag occupancy at the 48a Li site, and fully relaxed to a force tolerance of 0.01 eV /Å. The phase stability of these relaxed structures was assessed by calculating the energy above the convex hull (E^{hull})

using the Materials Project (MP) database[44]. The electrochemical exsolution of Ag was examined via the grand potential phase diagram, with the chemical potential μ_{Li} defined as[45]:

$$\mu_{Li}(\varphi) = \mu_{Li,0} - e\varphi \quad (1)$$

where $\mu_{Li,0}$ represents the chemical potential of Li metal, e is the elementary charge, and φ is the potential relative to the Li metal negative electrode. The chemical potential μ_{Li} is directly related to the potential vs. Li/Li^+, expressed as:

$$V = -\mu_{Li}/zF \quad (2)$$

where F is the Faraday constant, z is the number of electrons transferred ($z = 1$ for Li), and φ is referenced to the energy of Li metal. The pymatgen code was utilized to generate the grand potential phase diagrams and to identify stable compounds as a function of the chemical potential μ_{Li}. The thermodynamic tendency to decompose into its equilibrium phases was quantified by calculating the decomposition reaction energy, E_D, at a given potential φ as follows:

$$E_D = E(\text{phase equilibria}, \varphi) - E(Li_6PS_5Cl) - \Delta n\mu_{Li}(\varphi) \quad (3)$$

Here, E(phase equilibria, φ) represents the total energy of the equilibrium phases at the potential φ, $E(Li_6PS_5Cl, \varphi)$ is the energy of the Li_6PS_5Cl, and Δn_{Li} denotes the change in the number of Li atoms from the solid electrolyte composition to the equilibrium composition.

Ab initio molecular dynamics (AIMD) simulations were conducted to explore Ag diffusion within $Li_{6-x}Ag_xPS_5Cl$. These simulations were performed in the NVT ensemble using a Nose-Hoover thermostat at 1000 K, with a time step of 2 fs over a total simulation time of 400 ps. The Γ-point only sampling of k-space was used. The atomic trajectories of Li and Ag were visualized and analyzed using the Open Visualization Tool (OVITO) software.

Data availability

The data that support the findings of this study are available from the source data. Source data are provided in this paper.

References

1. Deiseroth, H.-J. et al. Li_6PS_5X: A class of crystalline Li-rich solids with an unusually high Li^+ mobility. *Angew. Chem. Int. Ed.* **47**, 755 (2008).
2. Kamaya, N. et al. A lithium superionic conductor. *Nat. Mater.* **10**, 682 (2011).
3. Mizuno, F., Hayashi, A., Tadanaga, K. & Tatsumisago, M. New, highly ion-conductive crystals precipitated from Li_2S-P_2S_5 glasses. *Adv. Mater.* **17**, 918 (2005).
4. Sakuda, A., Hayashi, A. & Tatsumisago, M. Sulfide solid electrolyte with favorable mechanical property for all-solid-state lithium battery. *Sci. Rep.* **3**, 2261 (2013).
5. Kim, K. J., Balaish, M., Wadaguchi, M., Kong, L. & Rupp, J. L. M. Solid-state Li–metal batteries: challenges and horizons of oxide and sulfide solid electrolytes and their interfaces. *Adv. Energy Mater.* **11**, 2002689 (2021).
6. He, B. et al. Halogen chemistry of solid electrolytes in all-solid-state batteries. *Nat. Rev. Chem.* **7**, 826 (2023).
7. Huang, W.-Z. et al. Anode-free solid-state lithium batteries: a review. *Adv. Energy Mater.* **12**, 2201044 (2022).
8. Xie, C. et al. Regulating Li nucleation and growth heterogeneities via near-surface lithium-ion irrigation for stable anode-less lithium metal batteries. *Small* **20**, 2306868 (2024).
9. Zor, C., Turrell, S. J., Uyanik, M. S. & Afyon, S. Lithium plating and stripping: toward anode-free solid-state batteries. *Adv. Energy Sustain. Res.* **5**, 2300001 (2023).
10. An, Y., Zeng, Y., Luan, D. & Lou, X. W. Materials design for high-energy-density anode-free batteries. *Matter* **7**, 1466 (2024).
11. Kazyak, E. et al. Understanding the electro-chemo-mechanics of Li plating in anode-free solid-state batteries with operando 3D microscopy. *Matter* **5**, 3912 (2022).
12. Lewis, J. A. et al. Linking void and interphase evolution to electrochemistry in solid-state batteries using operando X-ray tomography. *Nat. Mater.* **20**, 503 (2021).
13. Sandoval, S. E. et al. Structural and electrochemical evolution of alloy interfacial layers in anode-free solid-state batteries. *Joule* **7**, 2054 (2023).
14. Ning, Z. et al. Dendrite initiation and propagation in lithium metal solid-state batteries. *Nature* **618**, 287 (2023).
15. Han, F. et al. High electronic conductivity as the origin of lithium dendrite formation within solid electrolytes. *Nat. Energy* **4**, 187 (2019).
16. Singh, D. K. et al. Li_6PS_5Cl microstructure and influence on dendrite growth in solid-state batteries with lithium metal anode. *Cell Rep. Phys. Sci.* **3**, 101043 (2022).
17. Tian, H.-K., Liu, Z., Ji, Y., Chen, L.-Q. & Qi, Y. Interfacial electronic properties dictate Li dendrite growth in solid electrolytes. *Chem. Mater.* **31**, 7351 (2019).
18. Kasemchainan, J. et al. Critical stripping current leads to dendrite formation on plating in lithium anode solid electrolyte cells. *Nat. Mater.* **18**, 1105 (2019).
19. Wan, H., Wang, Z., Zhang, W., He, X. & Wang, C. Interface design for all-solid-state lithium batteries. *Nature* **623**, 739 (2023).
20. Wang, M. J., Choudhury, R. & Sakamoto, J. Characterizing the Li-solid-electrolyte interface dynamics as a function of stack pressure and current density. *Joule* **3**, 2165 (2019).
21. Fuchs, T. et al. Imaging the microstructure of lithium and sodium metal in anode-free solid-state batteries using electron backscatter diffraction. *Nat. Mater.* **23**, 1678 (2024).
22. Lu, Y. et al. The void formation behaviors in working solid-state Li metal batteries. *Sci. Adv.* **8**, eadd0510 (2022).
23. Zhou, L., Minafra, N., Zeier, W. G. & Nazar, L. F. Innovative approaches to Li-argyrodite solid electrolytes for all-solid-state lithium batteries. *Acc. Chem. Res.* **54**, 2717 (2021).
24. Schlenker, R. et al. Structure and diffusion pathways in Li_6PS_5Cl argyrodite from neutron diffraction, pair-distribution function analysis, and NMR. *Chem. Mater.* **32**, 8420 (2020).
25. Li, Y. et al. Interface stability of LiCl-rich argyrodite Li_6PS_5Cl with propylene carbonate boosts high-performance lithium batteries. *Electrochim. Acta* **363**, 137128 (2020).
26. Hota, G., Idage, S. B. & Khilar, K. C. Characterization of nano-sized CdS–Ag_2S core-shell nanoparticles using XPS technique. *Colloids Surf. A Physicochem. Eng.* **293**, 5 (2007).
27. Tan, D. H. S. et al. Elucidating reversible electrochemical redox of Li_6PS_5Cl solid electrolyte. *ACS Energy Lett.* **4**, 2418 (2019).
28. Sun, W. et al. The thermodynamic scale of inorganic crystalline metastability. *Sci. Adv.* **2**, e1600225 (2016).
29. Zhou, J. et al. Healable and conductive sulfur iodide for solid-state Li–S batteries. *Nature* **627**, 301 (2024).
30. Park, C.-M., Jung, H. & Sohn, H.-J. Electrochemical behaviors and reaction mechanism of nanosilver with lithium. *Electrochem. Solid State Lett.* **12**, A171 (2009).
31. Ye, Y. et al. Solid-solution or intermetallic compounds: Phase dependence of the Li-alloying reactions for Li-metal batteries. *J. Am. Chem. Soc.* **145**, 24775 (2023).
32. Spencer-Jolly, D. et al. Structural changes in the silver-carbon composite anode interlayer of solid-state batteries. *Joule* **7**, 503 (2023).
33. Zhu, Y., He, X. & Mo, Y. Origin of outstanding stability in the lithium solid electrolyte materials: insights from thermodynamic analyses

based on first-principles calculations. *ACS Appl. Mater. Interfaces* **7**, 23685 (2015).
34. Schwietert, T. K. et al. Clarifying the relationship between redox activity and electrochemical stability in solid electrolytes. *Nat. Mater.* **19**, 428 (2020).
35. Lee, Y.-G. et al. High-energy long-cycling all-solid-state lithium metal batteries enabled by silver–carbon composite anodes. *Nat. Energy* **5**, 299 (2020).
36. Hanghofer, I. et al. Fast rotational dynamics in argyrodite-type Li_6PS_5X (X: Cl, Br, I) as seen by ^{31}P nuclear magnetic relaxation – on cation-anion coupled transport in thiophosphates. *Chem. Mater.* **31**, 4591 (2019).
37. Yu, T. et al. A prototype of dual-ion conductor for all-solid-state lithium batteries. *Sci. Adv.* **9**, eadj8171 (2023).
38. Liu, X. et al. Local electronic structure variation resulting in Li 'filament' formation within solid electrolytes. *Nat. Mater.* **20**, 1485 (2021).
39. Quirk, J. A. & Dawson, J. A. Design principles for grain boundaries in solid-state lithium-ion conductors. *Adv. Energy Mater.* **13**, 2301114 (2023).
40. Kresse, G. & Furthmüller, J. Efficient iterative schemes for ab initio total-energy calculations using a plane-wave basis set. *Phys. Rev. B* **54**, 11169 (1996).
41. Kresse, G. & Joubert, D. From ultrasoft pseudopotentials to the projector augmented-wave method. *Phys. Rev. B* **59**, 1758 (1999).
42. Perdew, J. P., Burke, K. & Ernzerhof, M. Generalized gradient approximation made simple. *Phys. Rev. Lett.* **77**, 3865 (1996).
43. Ong, S. P. et al. Python Materials Genomics (pymatgen): A robust, open-source python library for materials analysis. *Comput. Mater. Sci.* **68**, 314 (2013).
44. Jain, A. et al. Commentary: The materials project: A materials genome approach to accelerating materials innovation. *APL Mater.* **1**, 011002 (2013).
45. Ong, S. P., Wang, L., Kang, B. & Ceder, G. Li-Fe-P-O2 phase diagram from first principles calculations. *Chem. Mater.* **20**, 1798 (2008).

Acknowledgements

This work was supported by the Ministry of Trade, Industry & Energy (MOTIE, Korea) (No. 20007045) and the National Research Foundation of Korea (NRF) funded by the Korean Government (MSIT) (RS-2023-00261543). J.W.C. acknowledges support from the Institute of Engineering Research (IOER), the Research Institute of Advanced Materials (RIAM) and the Institute for Battery Research Innovation (IBRI) at Seoul National University. This work was also supported by the National Research Council of Science & Technology (NST) grant by the Korea government (MSIT) (No. GTL24011-000).

Author contributions

S.H.C., W.C., H.P. and J.W.C. conceived the project and designed the experiments. C.H.B., J.O. and G.J.L. conducted the experiments. M.K., H.L. and H.P. carried out DFT simulations and data analysis. D.J.Y., Y.S.J., K.S.K. and J.S.Y. assisted with the analyses. S.H.C., W.C., H.P. and J.W.C. wrote the manuscript. All authors discussed the results and commented on the manuscript.

Competing interests

The authors declare no competing interests.

Additional information

Supplementary information The online version contains supplementary material available at https://doi.org/10.1038/s41467-025-61074-9.

Correspondence and requests for materials should be addressed to Seung Ho Choi, Woosuk Cho, Haesun Park or Jang Wook Choi.

Peer review information *Nature Communications* thanks Ieuan Seymour and the other anonymous reviewers for their contribution to the peer review of this work. [A peer review file is available.]

Reprints and permissions information is available at http://www.nature.com/reprints

Publisher's note Springer Nature remains neutral with regard to jurisdictional claims in published maps and institutional affiliations.

Open Access This article is licensed under a Creative Commons Attribution-NonCommercial-NoDerivatives 4.0 International License, which permits any non-commercial use, sharing, distribution and reproduction in any medium or format, as long as you give appropriate credit to the original author(s) and the source, provide a link to the Creative Commons licence, and indicate if you modified the licensed material. You do not have permission under this licence to share adapted material derived from this article or parts of it. The images or other third party material in this article are included in the article's Creative Commons licence, unless indicated otherwise in a credit line to the material. If material is not included in the article's Creative Commons licence and your intended use is not permitted by statutory regulation or exceeds the permitted use, you will need to obtain permission directly from the copyright holder. To view a copy of this licence, visit http://creativecommons.org/licenses/by-nc-nd/4.0/.

© The Author(s) 2025